International Journal of Hydrogen Energy 111 (2025) 238–250

Contents lists available at ScienceDirect

International Journal of Hydrogen Energy

journal homepage: www.elsevier.com/locate/he

Towards a comprehensive, high-fidelity, multi-physics simulation framework for alkaline water electrolyzers

Marco Dreoni [a], Francesco Balduzzi [a,*], Francesco Maria Ferro [b], Kevin Panichi [b], Eleonora Ponticorvo [b], Giovanni Ferrara [a], Alessandro Bianchini [a]

[a] Department of Industrial Engineering, Università Degli Studi di Firenze, Via di Santa Marta 3, 50139, Firenze, Italy
[b] McPhy Energy Italia Srl, Via Ayrton Senna 22, San Miniato, 56028, Italy

ARTICLE INFO

Handling Editor: Fanglin F. Chen

Keywords:
Alkaline electrolyzers
CFD
Multi-physics
Thermal analysis
Hydrogen

ABSTRACT

To enable the industrial upscaling of alkaline electrolyzers, a deeper understanding of all the different "physics" involved is needed. To this end, while the use of computational fluid dynamics (CFD) is essential, comprehensive 3D CFD models are still rare, with stack simulations often hampered by computational cost. The present study addresses this research gap by introducing a detailed multi-physics CFD model for alkaline electrolyzers, integrating two-phase flow, electrochemistry, thermal effects (including Faraday and Joule heat sources, plus reaction heating in the thermal equation) and interaction between anodic and cathodic half-cells. Moreover, unlike previous models, which simulate one cell alone, our approach allows for the simulation of any specific cell within the stack by enabling boundary conditions to be tailored for the positioning of the cell at hand. The model successfully replicated the expected fluid-dynamic and heating trend of a real-cell geometry and allowed highlighting critical areas for design improvement.

1. Introduction

Electrolysis-based hydrogen production is a promising solution for renewable energy storage, with alkaline water electrolyzers (AWEs) being cost-effective and industrially mature for large-scale green hydrogen generation. AWEs have low installation costs, around 500-1000 USD/kW (Rodríguez and Amores [1], Wang et al. [2]) and can work sufficiently well in dynamic operation typical of a coupling with the fluctuating output of renewables.

Overcoming challenges related to reducing energy consumption, costs, and maintenance, while boosting AWE efficiency and durability, is essential for expanding electrolysis in renewable energy storage applications. Precise physical modeling represents an important element in this context. One of the most widely used models was proposed by Ulleberg [3], which provides a mathematical description of the polarization curve with parameters fitted empirically. However, these models usually neither include geometric aspects, nor are capable of modelling those effects that depend on the complete design of the cell. Furthermore, the modeling of thermal effects is usually made with a lumped thermal capacitance model only.

The operation of an alkaline electrolyzer cells is significantly influenced by temperature, which impacts efficiency, voltage requirements, and overall performance. In particular, as temperature increases, the required cell voltage for electrolysis decreases. This reduction in voltage at higher temperatures leads to improved energy efficiency of the electrolyzer, as also showed by the simulations by Gao et al. [4]. Muhsen et al. also studied the impact of temperature on the current density, correlating it to other parameters such as electrode-diaphragm gap. They found out that, among the other factors analyzed, temperature ranked second, contributing for 29 % to the current variation, thus highlighting its crucial role in shaping the system's behavior [5]. On the other hand, local high temperature values, or hot spots, are to be avoided, since they can compromise the material resistance. Norazahar et al. highlight that in proton exchange membrane (PEM) electrolysis, hot spots at the anode, influenced by the quality and supply of water, can cause mechanical and chemical degradation, potentially leading to membrane drying due to excessive gas volume fraction. This phenomenon can significantly reduce cell lifespan [6]. While extensive studies on membrane degradation in PEM electrolysis exist, there remains a notable gap in such research for alkaline water electrolysis (AWE). The occurrence of hot spots is linked to the maldistribution of two-phase flow and current density. In Ref. [6] a large zone of lower liquid superficial velocities appears near the beginning of

* Corresponding author.
E-mail address: francesco.balduzzi@unifi.it (F. Balduzzi).

https://doi.org/10.1016/j.ijhydene.2025.02.298
Received 30 December 2024; Received in revised form 16 February 2025; Accepted 18 February 2025
Available online 25 February 2025
0360-3199/© 2025 The Authors. Published by Elsevier Ltd on behalf of Hydrogen Energy Publications LLC. This is an open access article under the CC BY-NC-ND license (http://creativecommons.org/licenses/by-nc-nd/4.0/).

Nomenclature

Acronyms

AWE	Alkaline Water Electrolyzers
CFD	Computational Fluid Dynamics
PEM	Proton Exchange Membrane
SOFC	Solid Oxide Fuel Cell
PPS	Polyphenylene Sulfide
USD	US Dollars
VF	Volume Fraction
VOF	Volume of Fluid

Greek symbols

α	volume fraction [−]
ρ	density [kg/m^3]
σ	electrical conductivity [S/m]
$\vec{\varphi}_i$	diffusion flux of the ith species [m/s]

Latin symbols

A	electrode area [m^2]
d_{H2}	mean hydrogen bubble diameter [μm]
d_{O2}	mean oxygen bubble diameter [μm]
e	specific internal energy [J/kg]
e^-	electrons
F	Faraday constant [A·s/mol]
$\vec{F}$	external body force [N]
$\vec{F}_d$	drag force [N]
$\vec{F}_{lift}$	lift force [N]
$\vec{F}_{td}$	turbulent dispersion force [N]
$\vec{F}_{vm}$	virtual mass force [N]
$\vec{F}_{wl}$	wall lubrication force [N]
$\vec{g}$	gravitational acceleration [m/s^2]
G°	standard Gibbs free energy [kJ/mol]
h	specific internal enthalpy [J/kg]
H°	standard enthalpy of formation [kJ/mol]
i	current density [A/m^2]
I	electric current [A]
$\vec{J}_i$	mass flux of the ith species [kg/(m^2·s)]
k	thermal conductivity [W/(m·K)]
$\dot{m}_{gl}$	mass transfer from gas to liquid phase [kg/(m^3·s)]
M_i	molecular mass of species i [kg/mol]
$\dot{M}_{H2}$	hydrogen molar flow [kg/(mol·s)]
$\dot{M}_{O2}$	oxygen molar flow [kg/(mol·s)]
N	total number of species [−]
p	pressure [Pa]
p_{bar}	pressure in bar [bar]
P_{cell}^{heat}	power dissipated as heat by the cell [W]
R_i	net rate of production of species by chemical reaction [kg/(m^3·s)]
S°	standard entropy of formation [kJ/(mol·K)]
S_F	Faraday energy [W/m^3]
S_h	heat source term [W/m^3]
S_i	rate of creation from the dispersed phase plus user-defined sources [kg/(m^3·s)]
S_J	Joule energy [W/m^3]
S_k	mass source term of the kth phase [kg/(m^3·s)]
S_R	chemical reaction energy [W/m^3]
T	temperature [K]
$\bar{\bar{T}}$	stress tensor [−]
U_{cell}	cell potential [V]
U_{rev}°	standard reversible potential [V]
U_{tn}°	standard thermoneutral potential [V]
$v, \vec{v}$	velocity value and vector [m/s]
v', v''	stoichiometric coefficients as reactant and product [−]
W_i	liquid or solid species i
Y_i	local mass fraction of ith species [−]
z_i	charge number of ith species [−]

Subscripts

(aq)	aqueous state
(g)	gasous state
ave	average
g	gas phase
i	ith chemical species
k	generic phase
l	liquid phase
r	rth reaction
var	variable

the channels. This zone coincides with the location of high gas volume fraction. Thus, the high extent of gas holdup appears to reduce the flow of the liquid phase, leading in turn to hot spots.

To mitigate fluid stagnation at the electrode (closely tied to gas volume fraction) optimization of flow patterns is critical. Mat et al. [7] further observe that electrolyte flow velocity increases gas release rates due to reduced bubble residence time on the electrode surface. Studies, such as [8,9], emphasize that uniform electrolyte flow is essential for efficient AWE operation, as it reduces energy consumption. Using a 3D numerical model, Gao et al. demonstrated that low velocities can lead to bubble stagnation and higher local gas volume fractions, which in turn lower local current densities and increase ohmic overpotentials [4].

Another challenge that water electrolysis faces is linked to safety risks associated with gas crossover or hydrogen leaking. The presence of hydrogen and oxygen in AWE systems presents a considerable explosion hazard, particularly when gas crossover occurs, leading to the formation of highly explosive mixtures. This risk is further amplified under high-pressure conditions, emphasizing the need for advanced control systems to regulate gas pressure and electrolyte flow. Moreover, due to its small molecular size and high diffusivity, hydrogen is highly susceptible to leakage, creating significant safety concerns. Being colorless and odorless, hydrogen leaks are challenging to detect, necessitating the use of advanced detection systems and strict safety protocols. This topic has been covered widely in the works conducted by Refs. [10,11], with particular focus on AWE cells. A step forward in the safety analysis was performed by Liu et al., proposing a coupled Bayesian network coupled with a CFD model for a PEM water electrolysis cell [12]. From this perspective, progressing in simulation technology could also be beneficial for dedicated risk studies.

In the literature, three-dimensional (3D) CFD modeling of cells is still rare and full stack simulations are too computationally expensive [4,8,9,13]. Lee et al. developed a CFD analysis method for an AWE powered by renewable energy using COMSOL and considering the cell as isothermal [9]. Hawkes et al. used a 3D CFD electrochemical model to study a high-temperature electrolysis stack of solid oxide fuel cell (SOFC) using the commercial code Fluent by ANSYS [14]. Olesen et al. developed a PEM 3D model that accounts for compressible, two-phase flow including species, heat, and charge transport in the anode and membrane [15]. Still, a full alkaline electrolyzer stack CFD analysis could not be found by the authors during the literature review.

The present study proposes a multi-physics 3D model of an entire alkaline electrolyzer cell that can be used to simulate any of the cells within the stack. To make a step forward with respect to the state-of-the-art, the scope of the new modeling scheme was to address all the

"physics" involved in electrolysis, from two-phase flow to electrochemistry and thermal characterization. One of the main goals of the current study is also to show how the different physics mutually interact, proving that a comprehensive model is necessary for more accurate simulations.

The effect of hydrogen and oxygen bubble coverage was included by introducing a variable current density definition as a function of the gas presence on the electrodes. Cell heating, derived from the inherent electrical resistances and reactions, was introduced thanks to three different source terms, i.e., Faraday and chemical reactions heating at the electrodes and Joule heating inside the cell. The porous, semi-permeable diaphragm was modeled with the aim of only allowing the electrolyte to pass, blocking the generated gas, while at the same time enabling a thermal communication between the two half-cells. Finally, through properly tailored boundary conditions, it was possible to simulate any of the cells in the stack to evaluate their overall behaviour and different performance; in fact, moving from the first to the last cells, they realistically undergo specific pressure jumps and mass flow conditions with respect to the theoretical case.

Despite lacking a direct validation (also because detailed measurements within the electrolyzer are hard to make), the base CFD modeling framework built for the study was previously assessed by the authors taking as case-study an electrochemical cell from the literature, on which experimental data were available [16,17].

The CFD approach developed in the current study is thought to represent future support to the design phase. At the present stage, for example, it assists the design of electrolyzers by detecting areas of gas stagnation and consequent hot spots. In this regard, the safety of the device can also be improved through a proper modification of the cell geometry. The industrial partner is already taking advantage of the simulation results to modify critical areas of the cell.

This paper comprises six sections, including this introduction. Section 2 describes the case-study electrolyzer used for the CFD modeling. Section 3 outlines the methodology and numerical model setup, detailing geometry, meshing, and the models and forces utilized in Fluent 2023 R1. Section 4 presents and discusses the findings obtained by applying the CFD model on the electrolyzer cells. Finally, Section 5 serves as a summary of the discussion, with an overview of the key points, and Section 6 concludes the study with the main takeaways.

2. Case-study electrolyzer

For the present study, a 50-kW alkaline water electrolyzer was selected, featuring a maximum hydrogen production rate of 10 Nm^3/h and an operating pressure of 9 bar. The electrolyzer's cells are of the traditional type, with the anode and the cathode positioned on opposite sides of the cell, separated by a central diaphragm to allow for hydroxide ion migration. Hydrogen and hydroxide ions are produced at the cathode via the hydrogen evolution reaction, as in Equation (1). The diaphragm, made of polyphenylene sulfide (PPS), is permeable only to liquids, allowing ions to flow towards the anode under the influence of the potential field. At the anode, an oxygen evolution reaction occurs, generating oxygen and allowing electrons to complete the circuit by returning to the cathode, as illustrated in Equation (2).

$$2H_2O_{(l)} + 2e^- \rightarrow H_{2\,(g)} + 2OH^-_{(aq)}. \quad (1)$$

$$2OH^-_{(aq)} \rightarrow \frac{1}{2}O_{2\,(g)} + H_2O_{(l)} + 2e^-. \quad (2)$$

The cell has a disk-shaped design. The electrolyte, a 20 wt% aqueous NaOH solution, enters from a common horizontal channel at the bottom, with a mass flow of around 500 L/h, and moves upward through the two half-cells separately. The current density ranges from 1000 to 5000 A/m^2 with operating temperatures from 50 °C to 70 °C. For confidentiality reasons, exact operating values cannot be disclosed. The stack has a total of 115 cells in series.

Gases produced in the half-cells are collected at the top via two separate channels. A functional diagram, showing the main components, is provided in Fig. 1. The area of the electrode enclosed between a quarter and three-quarters of the cell height was selected to be shown in the results section. In fact, for confidentiality reasons regarding the exact cell geometry, no full pictures can be provided.

The selection of the cell was facilitated by the collaboration with the industrial partner, which provided access to detailed geometric data. The choice was further motivated by its suitability for simulations, thanks to the compact design and streamlined components, as it does not include catalysts or porous media within the half-cells.

3. Methodology

For the required multi-physics analysis of the cell, a CFD modeling approach was employed. Given the steady-state operating conditions of the cell, steady calculations were considered adequate for this case study. The analysis was conducted in the ANSYS 2023 R1 environment and fluid dynamics simulations were carried out in Fluent, enabling integration of the electrochemical and thermals model within the overall fluid dynamics framework, with high computational accuracy.

3.1. Geometry

The geometry was created using the Design Modeler software of ANSYS package. The numerical domain for this study was built to represent the portion of the alkaline cell between the cathode and anode, as shown in Fig. 1. The geometry represents a full cell, a rarity in state-of-the-art CFD modeling for electrolysis, including both half-cells and the diaphragm that separates them, having a porosity of 0.6. The full-cell configuration geometry was created with the intent to simulate any of the cells of the stack, by applying specific boundary conditions as explained in Section 3.3.3.

A case without the diaphragm was also examined to assess its impact. Due to its porosity, the liquid velocity in the diaphragm region is nearly negligible, suggesting that this component can be omitted if the analysis focuses solely on fluid dynamics. However, the inclusion of the diaphragm proved crucial for accurately capturing the thermal distribution within the cell.

Two full-cell geometries were developed to simulate individual cells within the stack; the first, central, i.e. the 58th, and last, i.e. the 115th, were chosen for the simulations. Specifically, one geometry was designed to represent the 115th cell featuring a single inlet at the bottom and two outlets at the top. The second geometry represents the remaining 114, with both the bottom and top channels having one inlet and one outlet each, as illustrated schematically in Fig. 2. The last cell required specific geometric adjustments to its channels to accommodate its unique flow configuration. Beyond the three quoted cells, other cases were not simulated, as their inclusion would offer limited additional insights. Moreover, the high computational cost of simulating individual cells and the necessity for precise boundary condition calibration further justified focusing on such representative cases.

3.2. Mesh

A hexahedral mesh was created in the ANSYS Meshing environment, followed by a grid independence test to provide accurate modeling. As discussed in Ref. [18], modeling two-phase flows requires balancing gas bubble size and gas production layer thickness to determine the minimum grid thickness. For the case-study analysis, calculating the minimum necessary layer thickness at the electrode yielded a value of 60 μm, with a chosen bubble diameter of 20 μm, as clarified in Section 3.3.2. In Eulerian simulations, setting cell sizes smaller than the bubble diameter can lack physical relevance. Accordingly, different refinement levels were tested, as reported in Table 1, which presents the layer size and total number of cells for each case.

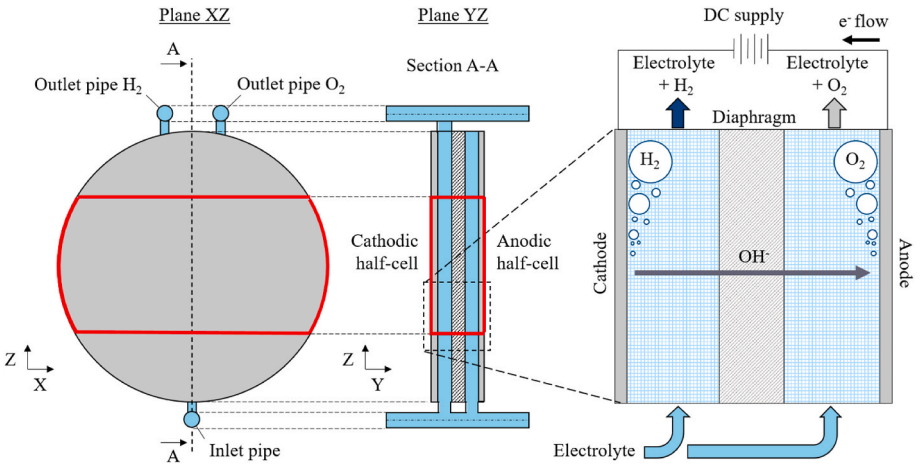

Fig. 1. Scheme of the case study alkaline electrolyzer cell. In red the results area. (For interpretation of the references to color in this figure legend, the reader is referred to the Web version of this article.)

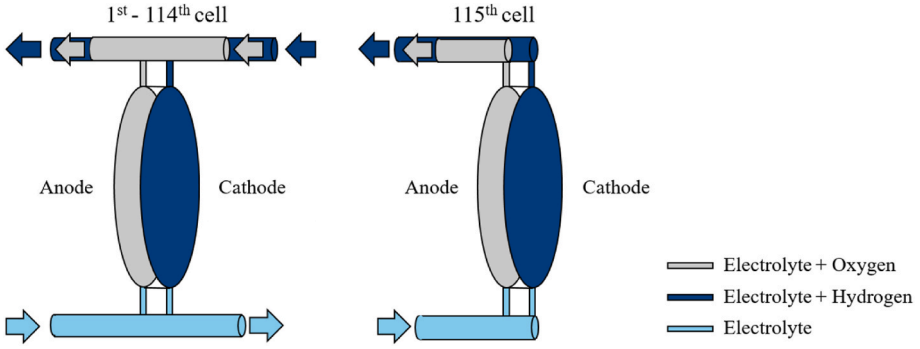

Fig. 2. Scheme of the two different geometries for the stack modeling.

Table 1
Features of the selected mesh sensitivity cases.

Mesh features	Mesh 1	Mesh 2	Mesh 3	Mesh 4
Layer size [μm]	100	120	200	240
Number of cells [−]	2.3E6	2E6	1E6	7.5E5

Fig. 3 presents the results for gas volume fraction (VF) and vertical velocity across the four mesh-sensitivity cases. Ultimately, "Mesh 2" was selected, offering sufficient accuracy.

It is evident how thinner layers at the electrode yield higher local gas volume fraction and consequent higher velocities. The two halves of the cell, cathodic on the left and anodic on the right, are also clearly separated by the diaphragm in the middle, where, as imposed for the simulations, both gas vertical velocity and VF are zero.

3.3. Fluid dynamics modeling

The flow in electrolyzer cells is characterized as a two-phase flow, consisting of a liquid electrolyte and gas bubbles generated at the electrodes. In CFD simulations, two main approaches are commonly employed to model such flows. The Euler-Lagrange method treats the electrolyte as a continuous phase and gas bubbles as discrete entities, while the Euler-Euler method represents both phases as interpenetrating

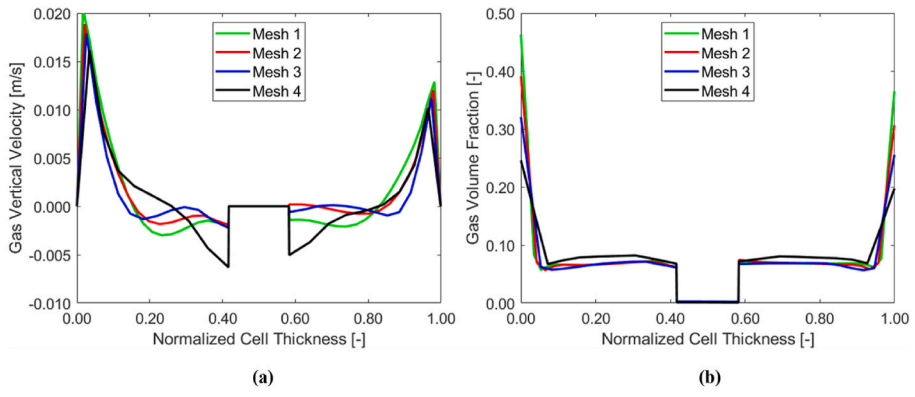

Fig. 3. Mesh sensitivity analysis: (**a**) gas vertical velocity and (**b**) VF along the cell thickness.

continua. More broadly, fluid motion can be described using two reference systems: fixed or moving. The Lagrangian approach focuses on individual particles within the continuum, tracking their motion over time. In contrast, the Euler-Euler approach describes fluid motion from a fixed spatial point, observing how different particles pass through this point over time.

Given the dispersed nature of the bubbles, the Euler-Euler method was selected for analysis. In particular, of the three available models in Fluent, i.e. Volume of Fluid (VOF), mixture and Eulerian model, the latter was selected, as it is deemed the most suitable and accurate for the current application.

An overview of the main momentum equations employed in the model is reported in Section 3.3.1. The main modeling hypotheses are provided in Section 3.3.2, whereas boundary conditions are presented in Section 3.3.3. Finally, Sections 3.3.4 and 3.3.5 focus on the electrochemical and thermal modeling aspects, respectively.

3.3.1. Eulerian model equations

The Eulerian model is the most complex of the multiphase models, since it solves a set of continuity equations for each phase. The mass continuity equations for the two-phase Eulerian model can be written for each phase as displayed in Equations (3) and (4), with subscript "l" referring to the liquid phase and subscript "g" to the gas phase [19]:

$$\frac{\partial}{\partial t}(\alpha_l \rho_l) + \nabla \bullet \left(\alpha_l \rho_l \vec{v}_l\right) = \left(\dot{m}_{gl} - \dot{m}_{lg}\right) + S_l, \tag{3}$$

$$\frac{\partial}{\partial t}(\alpha_g \rho_g) + \nabla \bullet \left(\alpha_g \rho_g \vec{v}_g\right) = \left(\dot{m}_{lg} - \dot{m}_{gl}\right) + S_g, \tag{4}$$

where α_k, ρ_k, $\vec{v}_k$, S_k are, respectively, the volume fraction, the density, the velocity, and the mass source term of phase "k", while $\dot{m}_{lg}$ and $\dot{m}_{gl}$ indicate the mass transfer from the liquid phase to the gas phase and vice versa. Equations (5) and (6) represent the momentum continuity equations for each phase [19]:

$$\begin{aligned}\frac{\partial}{\partial t}\left(\alpha_l \rho_l \vec{v}_l\right) + \nabla \bullet \left(\alpha_l \rho_l \vec{v}_l \vec{v}_l\right) &= -\alpha_l \nabla p + \nabla \\ \bullet \left(\alpha_l \bar{\bar{T}}_l\right) + \alpha_l \rho_l \vec{g} &+ \left(\vec{F}_{d,gl} + \dot{m}_{gl} \vec{v}_{gl} + \dot{m}_{lg} \vec{v}_{lg}\right) \\ + \left(\vec{F}_l + \vec{F}_{lift,l} + \vec{F}_{wl,l} + \vec{F}_{vm,l} + \vec{F}_{td,l}\right)&,\end{aligned} \tag{5}$$

$$\begin{aligned}\frac{\partial}{\partial t}\left(\alpha_g \rho_g \vec{v}_g\right) + \nabla \bullet \left(\alpha_g \rho_g \vec{v}_g \vec{v}_g\right) &= -\alpha_g \nabla p + \nabla \\ \bullet \left(\alpha_g \bar{\bar{T}}_g\right) + \alpha_g \rho_g \vec{g} &+ \left(\vec{F}_{d,lg} + \dot{m}_{lg} \vec{v}_{lg} + \dot{m}_{gl} \vec{v}_{gl}\right) \\ + \left(\vec{F}_g + \vec{F}_{lift,g} + \vec{F}_{wl,g} + \vec{F}_{vm,g} + \vec{F}_{td,g}\right)&,\end{aligned} \tag{6}$$

where p is the pressure shared between the two phases, $\vec{F}_l$ and $\vec{F}_g$ are external body forces, $\vec{F}_{d,gl} = -\vec{F}_{d,lg}$ is the drag force and $\vec{v}_{lg} = -\vec{v}_{gl}$ is the interphase velocity, $\vec{F}_{lift,l}$ and $\vec{F}_{lift,g}$ are the lift forces, $\vec{F}_{wl,l}$ and $\vec{F}_{wl,g}$ are the virtual mass forces, and $\vec{F}_{td,l}$ and $\vec{F}_{td,g}$ the turbulent dispersion forces. Finally, $\bar{\bar{T}}_l$ and $\bar{\bar{T}}_g$ are the stress tensors.

Coming to the species transport equation, Fluent predicts the local mass fraction of each species Y_i, through the solution of a convection-diffusion equation for the ith species. This conservation equation takes the general form of Equation (7) [19]:

$$\frac{\partial}{\partial t}(\rho_k Y_i) + \nabla \bullet \left(\rho_k \vec{v}_k Y_i\right) = -\nabla \bullet \vec{J}_i + R_i + S_i, \tag{7}$$

where R_i is the net rate of production of species by chemical reaction and S_i is the rate of creation by addition from the dispersed phase plus any user-defined sources. Finally, $\vec{J}_i$ represents the diffusion flux of the ith species, which arises due to gradients of concentration and temperature.

3.3.2. Modeling hypotheses

The following assumptions were made for the fluid-dynamic modeling.

- The inlet temperature and operating pressure were set to 52 °C and 9 bar, respectively, to align with real application conditions. A value of 70 °C was instead imposed as boundary conditions at the inlet for the channels on top of the cell, simulating the heated electrolyte and gas coming from preceding cells.
- Start-up operational conditions were also analyzed, setting a value of 52 °C at the inlet for the channels on top of the cell. Based on the available data, it takes several minutes to reach operational conditions. As a result, assuming a quasi-steady state was considered acceptable for the start-up analysis
- The primary phase is a 20 wt% NaOH solution in water, while the secondary phase is a mixture of hydrogen and oxygen: the gas mixture is a necessary selection to work with two-phase conditions on ANSYS Fluent. By calibrating the boundary conditions, authors were able to make sure only hydrogen was generated in the cathodic chamber and oxygen inside the anodic one.
- The flow regime was established as laminar due to the low velocities involved inside the cell, with a calculated Re of less than 1000.
- The bubble diameter for hydrogen and oxygen gas was kept constant at 20 μm. This reference value is based on the research presented in Ref. [20], which characterizes the mean bubble diameter as a function of working pressures ranging from 1 to 200 bar, according to the empirical Equations (8) and (9):

$$d_{H2} = 31.073\, p_{bar}^{-0.319}, \tag{8}$$

$$d_{O2} = 40.34\, p_{bar}^{-0.28}, \tag{9}$$

where d_{H2} and d_{O2} are the mean bubble diameters in μm for hydrogen and oxygen gas and p_{bar} is the pressure in bar. The average values from calculations are about 15 μm for hydrogen and 22 μm for oxygen. Given the need to select a bubble diameter for the entire gas mixture, the previously mentioned bubble size of 20 μm was chosen. More specifically, bubble diameter is employed by the software to calculate the Reynolds number and the drag force.

- Bubble coalescence and breakage were disregarded due to the locally high production rate of gas bubbles linked with the industrial current density values, compared to lab electrochemical cells that can be found in the literature, such as in Ref. [21]. This leads to small, dispersed bubbles due to the shorter time they spend on the electrode before detaching. Smaller bubbles generated at higher current densities typically have less surface instability and are less prone to breakage. A trend of the bubble diameter decreasing with the current density can be found in Ref. [22]. At the same time, smaller and more frequent bubble detachment reduces the likelihood of coalescence, as the bubbles may not have sufficient time to grow large enough to interact and merge with other bubbles nearby [23,24].
- Among the interface forces exchanged between the gas and liquid phases, the primary ones typically used to implement the Eulerian model are drag, lift, wall lubrication, and virtual mass forces. Wall lubrication model specifically controls the interaction between phases at the wall. For liquid-gas bubbly flows, using the Eulerian model, the effect of wall lubrication force on the secondary phase (bubbles) can be included in the modeling. Such force tends to push the gaseous phase away from walls.

In this study, the lift force was omitted, assuming the bubbles as spherical, small, and non-deformable, which is also recommended by

the solver's guidelines [19]. Ishii-Zuber formulation was chosen for drag force, Antal et al. modeling [25] for wall lubrication and a coefficient of 0.5 for the virtual mass force.

3.3.3. Boundary conditions

Regarding the boundary conditions, they were tailored to capture the distinct fluid-dynamic and thermal behaviors of the cells under various configurations.

The inlet mass flow rates were calculated individually for the three selected cells in the simulated stack to maintain a coherent electrolyte flow within the cell and channels. In particular, it was assumed that the electrolyte is uniformly distributed, meaning each cell receives an equal flow rate, calculated as the total flow divided by the number of cells. This assumption is reasonable, as the pressure drop in the collector channels of the stack is considered negligible due to the low velocities, which result from the large cross-sectional area relative to the narrow passages inside the cells. To accurately represent realistic operating conditions, gas volume fraction was prescribed at the inlets of the top channels for the 1st and 58th cells, simulating the fraction of hydrogen or oxygen carried over from preceding cells in the stack.

Outlet pressures were meticulously calibrated to ensure the desired flow rates and maintain operational stability across the cells. More specifically, calibration was conducted by monitoring the outlet mass flow rates and gas volume fractions, to be consistent with the ones expected for the selected cell.

No-slip boundary conditions were applied to the walls of both the cathode and anode compartments, ensuring that the liquid and gas phases adhered to the surfaces. For the diaphragm, a zero-gas-velocity condition was imposed, effectively modeling its semi-permeable nature and restricting gas flow through this component.

In the no-diaphragm configuration, the absence of the diaphragm was accounted for by imposing separate no-slip wall conditions for each half-cell.

3.3.4. Electrochemical modeling

Hydrogen and oxygen gas products were incorporated into the model by activating the available electrochemical module. The hydrogen and oxygen evolution reaction described in Equations (1) and (2) were applied at the cathode and anode electrodes, as wall conditions.

More specifically, the software employs the inputs given by the user, for the electrochemical reactions, to solve the following charge-transfer reaction (Equation (10) [19]):

$$\sum_{i=1}^{N} v'_{i,r} Y_i^{z_i} \leftrightarrow \sum_{i=1}^{N} v''_{i,r} Y_i^{z_i} + \left(\sum_{i=1}^{N} \left(v''_{i,r} - v'_{i,r} \right) z_i \right) e^{-}, \tag{10}$$

where Y_i represents liquid or solid species i, N is the total number of species, $v'_{i,r}$ and $v''_{i,r}$ are the stoichiometric coefficients of the ith species as reactant and product in the reaction r respectively, z_i is the charge number of the ith species, e^- represents the electrons. Fluent makes use of the reaction at a phase level, for liquid and gas species, independently.

Current density conditions are instead imposed at the walls at a mixture level. Specifically, a current density function was used at the electrodes, following the approach by the authors in Ref. [17], relating it to the local gas volume fraction:

$$i_{var} = i_{ave} \left(1 - \alpha_g\right) / \left(1 - \alpha_{g,ave}\right), \tag{11}$$

where i_{var} is the variable local current density, defined cell by cell; i_{ave} is the average electrode current density; α_g is the local volume fraction for the gas phase; and $\alpha_{g,ave}$ is the average electrode gas volume fraction, calculated for each iteration. In such way the impact of bubble coverage on the electrode is considered.

The software determines the volume of hydrogen and oxygen produced by applying Faraday's law (Equations (12) and (13)), taking into account the local values of current density:

$$\dot{M}_{H2} = \frac{iA}{Fz_{H2}}, \tag{12}$$

$$\dot{M}_{O2} = \frac{iA}{Fz_{O2}}, \tag{13}$$

where $\dot{M}_{H2}$ and $\dot{M}_{O2}$ represent the molar flows of hydrogen and oxygen respectively, i is the current density, A the active area of the electrode, F = 96,487 As/mol the Faraday constant, and z the number of electrons involved in the electrochemical reactions: $z_{H2} = 2$ for hydrogen generation, $z_{O2} = 4$ for oxygen generation, as can be derived from Equations (1) and (2).

3.3.5. Thermal modeling

The decomposition of water is an endothermic process with a significant energy demand, as indicated by the standard enthalpy change associated with the electrolysis reaction, $\Delta H^\circ = 286$ kJ/mol (equivalent to 39.7 kWh/kg of H_2) [26]. At standard conditions (1 atm and 25 °C), the minimum energy required to decompose water corresponds to the change in Gibbs free energy ($\Delta G^\circ = 237$ kJ/mol). This energy requirement can also be expressed in terms of voltage:

$$\frac{\Delta G^\circ}{z_{H2} F} = \frac{237,000 \text{ J}}{2 \bullet 96,485 \text{ C}} = 1.23 \text{ V} = U^0_{rev}, \tag{14}$$

where U°_{rev} is the reversible potential, representing the minimum energy required in the form of electricity to drive water electrolysis. The additional energy needed to reach ΔH°, the total energy demand, with corresponding voltage known as the thermoneutral potential, U°_{tn} in Equation (15), can be supplied as heat, $T \cdot \Delta S^\circ$ in Equation (16), if the system operates at a sufficiently high temperature:

$$\frac{\Delta H^\circ}{z_{H2} F} = \frac{286,000 \text{ J}}{2 \bullet 96,485 \text{ C}} = 1.48 \text{ V} = U^\circ_{tn}, \tag{15}$$

$$T \bullet \Delta S^\circ = \Delta H^\circ - \Delta G^\circ, \tag{16}$$

where ΔS° is the entropy change associated with the electrolysis reaction. The total energy demand, ΔH°, changes with temperature, decreasing slightly from 286 kJ/mol at 25 °C to 283 kJ/mol (associated with a thermoneutral voltage of 1.47 V) at 100 °C and 278 kJ/mol (1.44 V) at 250 °C [27]. However, as the entropy increases during water decomposition, the term $T \cdot \Delta S^\circ$ grows substantially with temperature, allowing a larger fraction of the energy to be supplied as heat. In turn, the minimum electrical energy required decreases, as reflected in the decline of the reversible potential, U°_{rev}, with increasing temperature. Specifically, U°_{rev} drops from 1.23 V at 25 °C to 1.17 V at 100 °C and further to 1.05 V at 250 °C [27].

The operating electric potential of an electrolysis cell, U_{cell}, is greater than the reversible potential, U°_{rev}, due to process inefficiencies, such as overpotentials and resistive losses, leading to a reduction in overall efficiency. The cell potential can reach values going from less than 1.8 V in advanced alkaline electrolyzers [28] to values above 2 V. In their work, Benghamen et al. indicated a range going from 1.5 to 2.6 V for alkaline electrolyzers operating up to 200 bar [29]. This electric potential significantly exceeds the thermoneutral voltage, resulting in the release of heat during water electrolysis, despite the process being inherently endothermic. The waste heat associated allows maintaining the electrolysis temperature and it is produced at a rate directly proportional to the difference between the actual cell potential and the thermoneutral voltage. Power dissipated as heat was characterized as in Equation (17), by Diéguez et al. [26] and Sakas et al. [30], following the modeling in Ref. [3]:

$$P^{heat}_{cell} = I \bullet \left(U_{cell} - U_{tn}\right), \tag{17}$$

where P^{heat}_{cell} (W), is the power dissipated as heat in a water electrolysis

cell working with an electric current I (A) and a difference of potential U_{cell} (V) between anode and cathode.

Coming to the present numerical study, the thermal modeling lies on the energy equation, Equation (18), used by Fluent solver for both phases [19]:

$$\frac{\partial}{\partial t}\left(\rho\left(e+\frac{v^2}{2}\right)\right)+\nabla\cdot\left(pv\left(h+\frac{v^2}{2}\right)\right)=\nabla\cdot\left(k\nabla T-\sum_i h_i\vec{J}_i+\bar{\bar{T}}\cdot\vec{v}\right)+S_h, \tag{18}$$

where e is the specific internal energy, h is the specific internal enthalpy, k is the thermal conductivity, $\vec{J}_j$ is the diffusion flux of species i, $\bar{\bar{T}}$ is the stress tensor and S_h represents the heat sources. For the present analysis, three sources of energy were considered, to characterize the heat power of Equation (11), i.e. the energy related to the chemical reactions, the faradaic energy linked to the overpotentials occurring at the electrodes and the Joule energy involving the whole cell and related to the resistance encountered by the charged species. This thermal setup was based on the guidelines provided in Ref. [19], although no additional references in the literature were found to support this approach. More specifically, the chemical reaction energy is primarily associated with the enthalpy change of the water-splitting reaction. As the electrolysis process takes place, heat is generated due to the exothermic nature of the reaction. The effective heat generation can vary significantly depending on operational conditions (temperature and pressure) and can be influenced by the efficiency of the cell. It is calculated by the solver as in Equation (19) [19]:

$$S_R=\sum_i H_i^0\frac{R_i}{M_i}, \tag{19}$$

where H_i^0 is the enthalpy of formation, R_i volumetric rate of creation and M_i the molecular mass of species i.

Faradaic and Joule heat sources can be defined with Equations (20) and (21) [19]:

$$S_J=i^2/\sigma, \tag{20}$$

$$S_F=i\Delta U, \tag{21}$$

where σ is the electrical conductivity and ΔU the total cell overpotential. Joule heating (or resistive heating) generates from the electrical resistance within the electrolyzer, while Faradaic heating arises from the energy dissipated during electrochemical reactions at the electrodes, thus it is closely linked to the current density and efficiency of the electrochemical reactions. Joule heating typically plays a dominant role in thermal management due to its dependence on current flow and resistance.

To provide an idea of the order of magnitude of such heating components, Joule heating, at industrial current densities average values, can be up to several hundred W/m^2 and it is significantly higher than the other heating sources, due to its dependence on the square of the current density.

4. Results

4.1. Comparison between the full cell with diaphragm and two separate half-cells

The described multi-physics model was initially applied to the central cell of the stack, namely the 58th cell, considered representative of the average cell behavior. As a first analysis, authors assessed the criticality related to incorporating the diaphragm inside the cell geometry. Focus was given to the temperature distribution within the cell, comparing scenarios with and without such component to assess its impact. Fig. 4 (a) and (b) show the temperature contours on the vertical transversal YZ plane for the central section of the cell, as defined in Fig. 1, for the cases without and with diaphragm, respectively. Results clearly show that the anodic cell temperature on the left is higher than the cathodic cell temperature on the right, as also confirmed by the charts in Fig. 5. This is primarily due to the difference in specific heat capacities between oxygen and hydrogen: oxygen has a specific heat around 1000 J/kg K, whereas hydrogen's is approximately 14,000 J/kg K and electrolyte's 3300 J/kg K. As a result, the temperature rises more significantly in the anodic half-cell than in the cathodic one. The importance of the diaphragm component in thermal analysis becomes evident when comparing the two cases for both temperature and gas volume fraction variables. The diaphragm configuration promotes more uniform temperature distribution throughout the cell domain. Maximum temperatures measured at the anode reach values of 353 K without diaphragm, against 343 K with such component. Furthermore, when analyzing the gas volume fraction, it becomes evident that not including the diaphragm leads to higher gas accumulation, as evident in Fig. 4(c) and (d). The variation in the volume fraction contour can be attributed to the slight gas intrusion into the diaphragm, particularly in the cathodic half-cell [31,32]. In fact, according to the industrial partner, around 1 % of hydrogen impurity in the oxygen can be detected, due to the higher permeability of hydrogen molecules. On the other hand, oxygen permeates towards the cathode with more difficulty. For such reasons, higher gas stagnation inside the cell takes place in the no-diaphragm configuration, which is also a probable driver for the higher temperature measured in this case.

The three charts of Fig. 5(a) and (b) and (c) illustrate the temperature distribution trends along the thickness of the cell with the diaphragm (red curves) and without a diaphragm (blue curves), with continuous lines representing the liquid phase (phase 1), and the dashed lines used for gas phase (phase 2). The three panels correspond to different vertical sections of the cell, progressing from the bottom to the top. In particular, the first is taken at a quarter of the cell height, the second in the middle, and the third at three quarters of it.

In the lower part of the cell, the liquid phase shows a higher temperature for the diaphragm case compared to the non-diaphragm configuration. For the gas phase, the curve related to the diaphragm configuration exhibits a sharper temperature increase compared to one of the no-diaphragm case, suggesting that the diaphragm has a strong

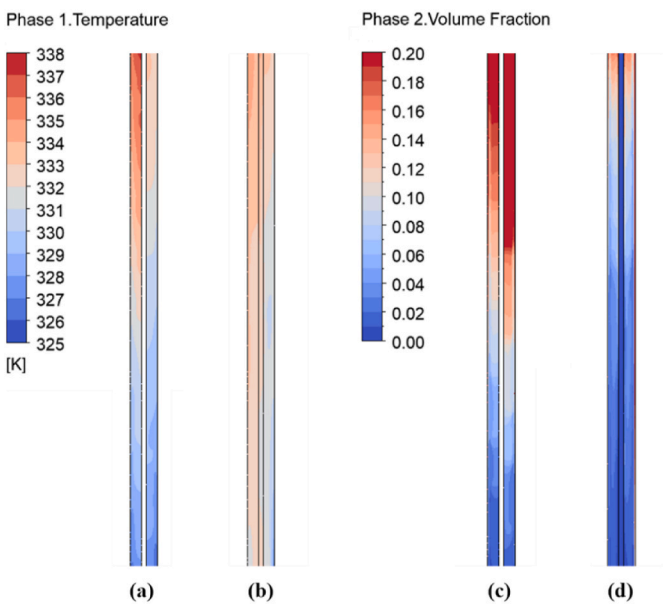

Fig. 4. Temperature contours, (**a**) without and (**b**) with diaphragm, and VF contours, (**c**) without and (**d**) with diaphragm, in 58th cell mid-section.

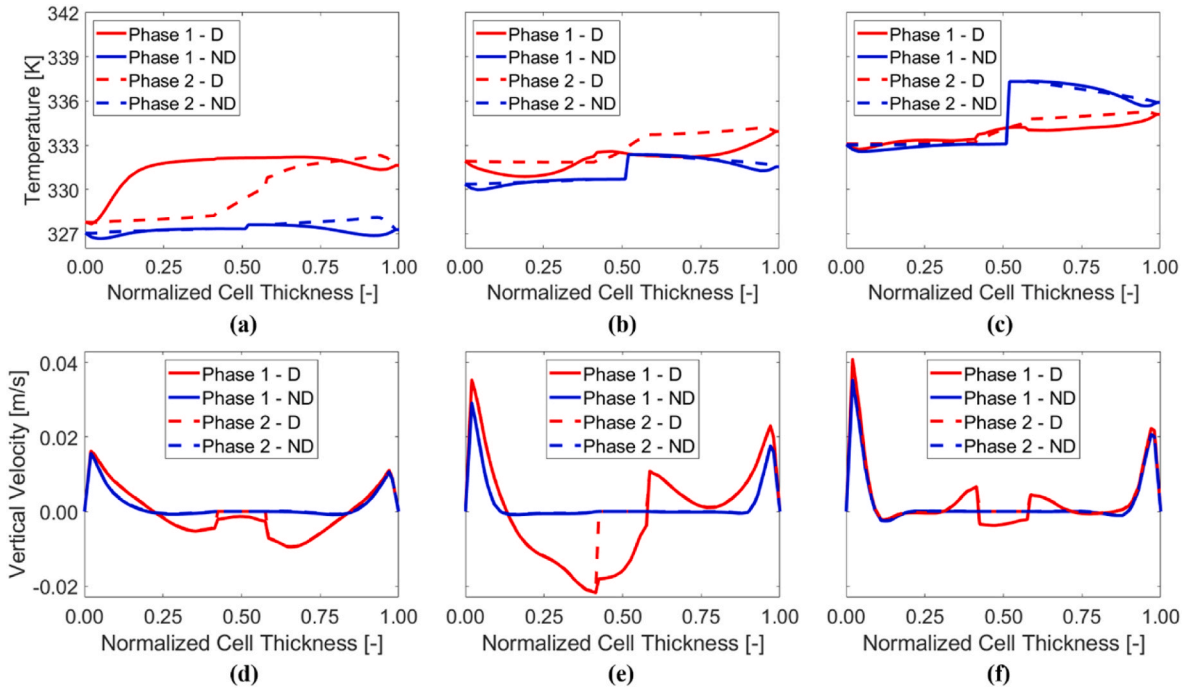

Fig. 5. Temperature **(a), (b), (c)** and vertical velocity **(d), (e), (f)** trends inside the cell, with and without diaphragm for the two phases: **(a)** temperature and **(d)** vertical velocity evaluated at a quarter cell height section; temperature **(b)** and **(d)** vertical velocity evaluated at half cell height section; temperature **(c)** and **(f)** vertical velocity evaluated at three-quarters cell height section.

impact on both phases.

In the middle of the cell, the temperatures for both liquid and gas phases increase compared to the bottom section. As expected, the heating sources start having a visible effect on the thermal output. The average temperature at this section of the cell is comparable for both cases and phases, being around 7 K higher than the inlet electrolyte temperature, of 325.15 K. The trends for the gas phase are smoother here compared to the bottom, showing a more distributed thermal profile. At the top of the cell, both liquid and gas phases show higher overall temperatures compared to the lower sections, reflecting the natural heat accumulation as the fluids ascend. The diaphragm case still exhibits higher temperatures in the cathodic chamber, while the anodic half-cell temperatures are on average 3 K higher for the non-diaphragm case.

To better understand the overall thermal behaviour along the cell height, it is necessary to consider the vertical velocity patterns inside the half-cells. Fig. 5(d) and (e) and (f) illustrate such variable, for the same vertical sections of the cell.

It is evident how recirculation, represented by the peaks of downwards vertical velocity, is enhanced for the diaphragm case. This evidently leads to the higher mixing and temperature uniformity along the cell that can be noticed in Fig. 5 (a), (b), (c). For such reasons, full cell modeling is more physically accurate than simulating isolated half-cells, particularly for thermal study purposes. Results presented in the following paragraphs always include the diaphragm component.

4.2. Comparison among different cells of the stack

As already explained in Section 3.1, the nominal work conditions of the first, central, and last cells of the stack were simulated, with the fluid-dynamic modeling described. Fig. 6 illustrates the gas volume fraction at the anode and cathode for each of the three cells, on a vertical plane parallel to plane XZ, as defined in Fig. 1. It can be observed that the overall pattern is quite similar among the cells. Table 2 provides the average values of volume fraction, revealing an average of about +30% higher gas volume fraction at the cathode compared to the anode. This difference appears to be independent of the specific cell geometry, as it persists in the last cell (the 115th cell) as well. For each configuration maximum values of gas VF tend to 1 inside the cathodic half-cell, in

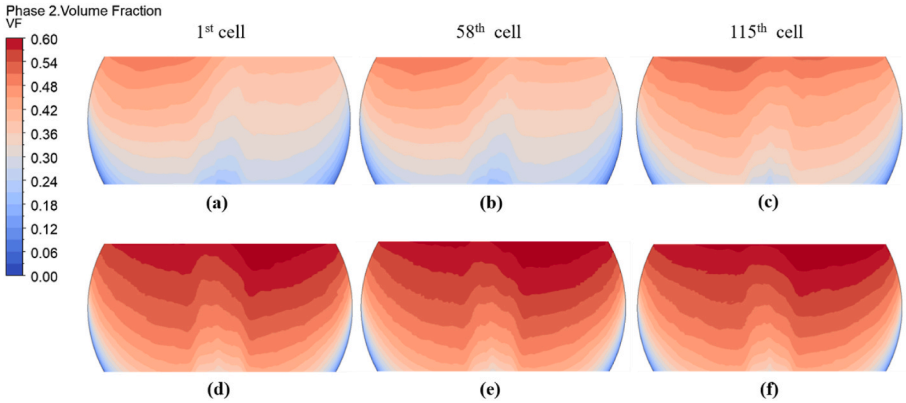

Fig. 6. Anode gas VF: (**a**) first, (**b**) central and (**c**) last cell. Cathode gas VF: (**d**) first, (**e**) central and (**f**) last cell.

Table 2
Average gas volume fraction values at the electrodes for the different cells.

Variables	Cell 1	Cell 58	Cell 115
Average gas VF at the anode [−]	0.34	0.34	0.39
Average gas VF at the cathode [−]	0.48	0.48	0.48

specific areas at the top where the gas can accumulate, also representing a potential issue of hot spots and consequent material damage.

To understand the reason behind the difference of gas volume fraction between cathodic and anodic half-cells, several factors must be considered. First, hydrogen's lower density compared to oxygen results in greater buoyancy forces and velocities in the cathodic cell, even though the total molar flow, based on Faraday's law, is higher for oxygen at the anode. This is consistent with higher velocities observed near the cathode, which is visible in Fig. 5 (d), (e), (f). The higher velocities near the cathode lead to increased recirculation when the flow reaches the cell top, creating vorticity. The simulations show values of enhanced downwards velocities for the cathodic half-cell compared to the anodic ones, as also particularly evident from Fig. 5 (e). Such vorticity and recirculation contribute to the higher gas VF at the cathode if the gas struggles to escape as easily as it does in the anodic chamber, where maximum velocities and recirculation are more moderate.

The volume fraction is slightly different between the first and central cells. This evidence can be attributed to electrolyte flow dynamics; simulations indeed indicate almost zero electrolyte flow through the central cell, likely due to a weaker Venturi effect compared to the first cell, where more electrolyte flows through the top channels. Conversely, the last cell has a unique geometry with a distinct fluid path, featuring only one inlet and two half-cell outlets; therefore, a different flow dynamic behaviour is expected inside such cell, with a direct influence on the overall volume fraction distribution.

More specifically, when analyzing the gas VF trends on a central line at anode and cathode, in Fig. 7 (a), it becomes clearer that the first and central cells exhibit very similar behaviors. In Fig. 7 (b) is instead presented the trend of the current density, normalized over the average current density for confidentiality reasons. Such variable follows the gas volume fraction trend in accordance with Equation (5), developed by the authors to introduce the impact of bubble coverage. Higher values of VF correspond to lower values of current density and vice versa. Interestingly, the gas VF pattern at the cathode for the last cell aligns closely with the other two cells, whereas a noticeable divergence is observed at the anode. This difference can be attributed to the flow dynamics at the half-cell inlets for the three cases.

Fig. 8 presents the liquid vertical velocity for the three cells on the vertical transversal YZ plane for the central section of the cell, as defined in Fig. 1. The contours in Fig. 8 reveal asymmetrical flow entry into the anodic chamber for the 1st and 58th cells, unlike the more balanced flow visible in the 115th cell. This asymmetry in the first and central cells arises because of their open inlet channels, with liquid motion mainly induced by the buoyancy-driven fluid movement of the generated gas. Conversely, the last cell geometry creates higher flow rates in the anodic half-cell due to the inlet channel being sealed at the end, redirecting the flow into the anodic chamber more easily. This design distinction impacts the fluid and gas distribution, particularly at the anode, and it is considered the main reason of the anodic gas VF difference among cells.

Coming to the thermal analysis, the contours of Fig. 9 illustrate average anodic and cathodic temperature distribution, on a plane parallel to XZ plane of Fig. 1. Average and maximum values are reported in Fig. 10. Given that the same heating sources apply across all three cases and both electrodes, we would expect similar temperature trends. However, the anode consistently shows higher temperatures on average, with even greater values going towards the first cells. This temperature disparity can likely be explained by the velocity non-uniformity analyzed in Fig. 8: lower velocities result in higher temperatures due to reduced fluid flow, which causes localized heating. It is noticeable that the maximum values of temperature for the first cell reach values 15 °C higher than we would expect, with clear hot spots at the sides of the cell where the flow stagnates. Maximum values are higher at the cathode than at the anode and this appears to go against what has already been said. However, this anomaly is strictly linked to the higher gas volume fraction at the cathode, since gas accumulation leads to local peaks of temperature, in specific areas of the electrode which are not visible in the displayed regions.

The chart in Fig. 11 illustrates the temperature trend on the electrodes for a central line. The higher average temperatures for the anode is here confirmed. Comparing it to the previous results, we can get to the general conclusion that the lower velocities at entrance of the half-cells lead to higher temperatures at the electrode. The temperature trend is also in line with the chart of Fig. 7 (b) where higher current densities in the lower part of the cell were highlighted, that can be consequently associated with local higher heating.

The charts in Fig. 12 show the electrolyte temperature and vertical velocity trends for the same three sections as in Fig. 5. Along the cell, lower temperature values for the 115th cell are visible in Fig. 12(a) and (b) and (c). This allows us to conclude that the lower temperature values, compared to the other cells, are not only characteristic of the electrodes, as already shown in Fig. 11, but of the overall cell domain. One of the reasons of this behaviour can be found in analyzing the values of charts (d), (e) and (f) with overall lower maximum velocities inside the cell and lower recirculation for the last cell, hindering thermal mixing. The cathodic half-cell 58 exhibits enhanced recirculation compared to the others, as evident in Fig. 12 (e), but also, less predominantly, in Fig. 12 (d). Simulations highlight how the different boundary conditions from cell to cell influence the flow distribution inside the half-cells, which have an impact on the overall electrolyte movement and can be the reason of high variability when analyzing the vertical velocity trends. Cell 58th temperature in the bottom part of the cell is clearly higher than the others (Fig. 12 (a)) as a probable cause of

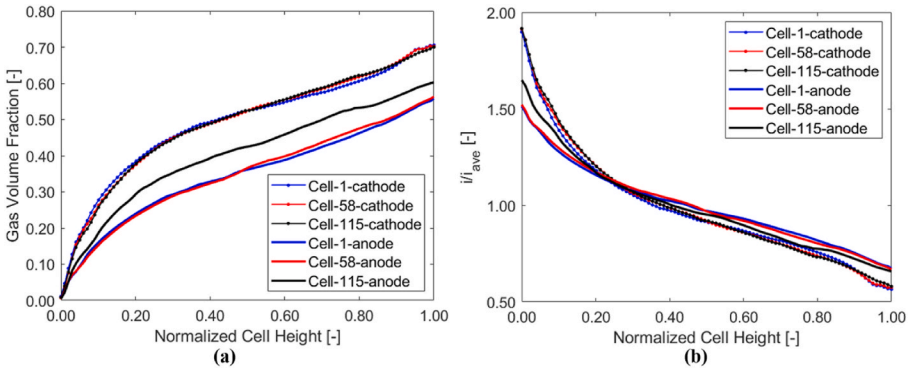

Fig. 7. Anode and cathode gas VF **(a)** and relative current density **(b)** for first, central and last cell.

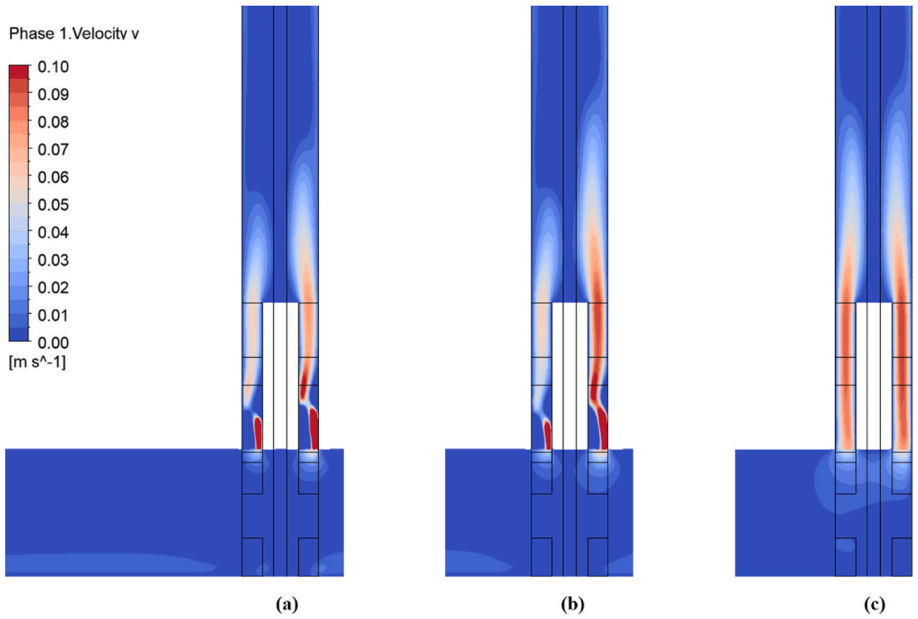

Fig. 8. Liquid vertical velocity contour in the low part of the cell: first **(a)**, central **(b)**, and last **(c)** cell.

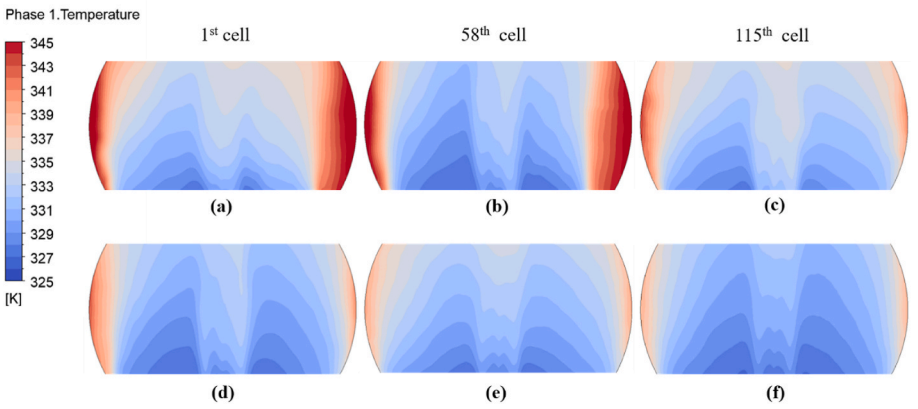

Fig. 9. Anode temperature: (**a**) first, (**b**) central and (**c**) last cell. Cathode temperature: (**d**) first, (**e**) central and (**f**) last cell.

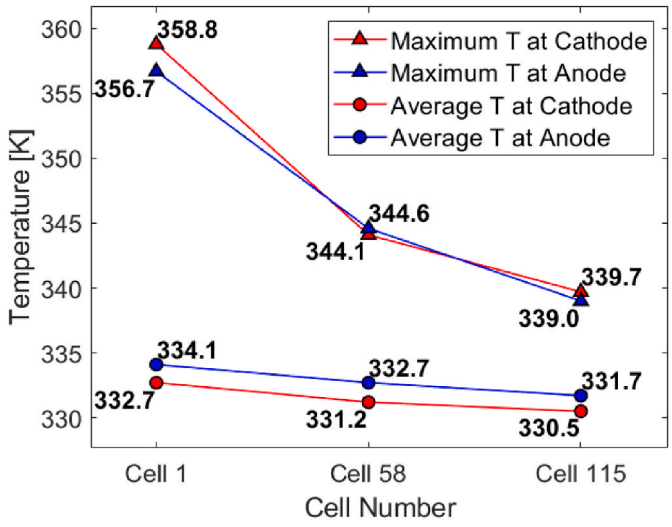

Fig. 10. Average and maximum temperature values at the electrodes for the different cells.

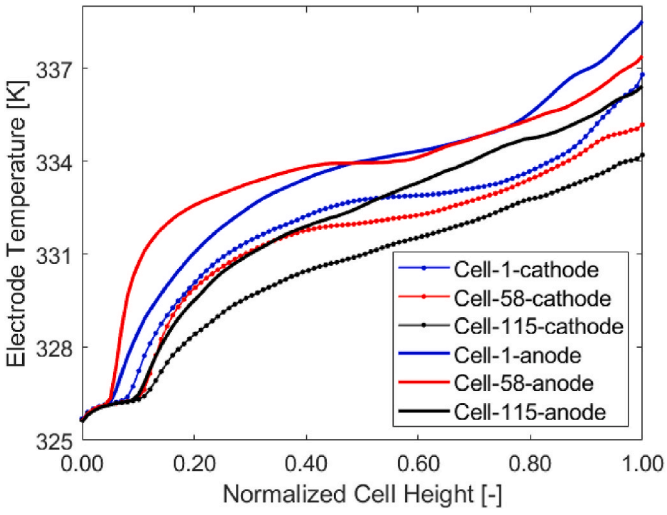

Fig. 11. Anode and cathode temperature for first, central and last cell.

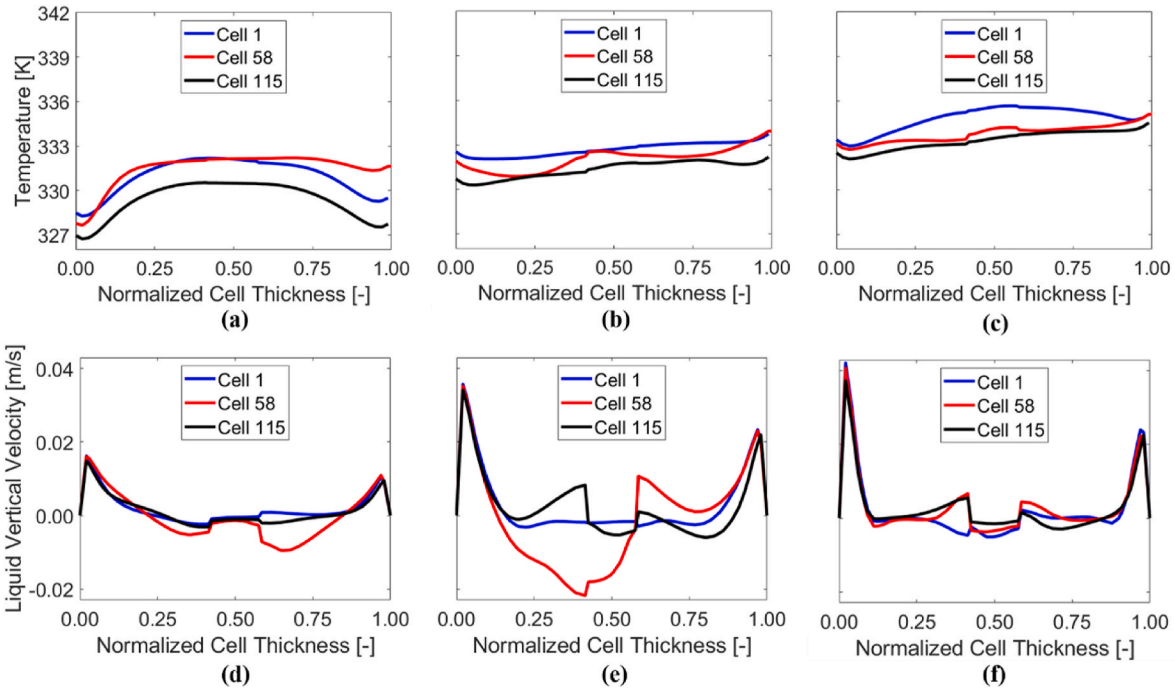

Fig. 12. Electrolyte temperature **(a), (b), (c)** and vertical velocity **(d), (e), (f)** trends inside the cell for 1st, 58th and 115th cells: **(a)** temperature and **(d)** vertical velocity evaluated at a quarter cell height section; temperature **(b)** and **(d)** vertical velocity evaluated at half cell height section; temperature **(c)** and **(f)** vertical velocity evaluated at three-quarters cell height section.

the high recirculation described.

The notable difference in peak temperature between the last cell and the other cells can also be attributed to the influence of the top channels' temperature. In the simulation, a top channel temperature of 343.15 K (70 °C) was imposed for cells 1 and 58, due to the expected heat generation inside the preceding cells, as already anticipated in Section 3.3.2. When the top channel temperature was instead set to 325.15 K (52 °C), the expected inlet temperature at start-up, the maximum temperature values reduced, as illustrated in Fig. 13, where anode and cathode temperature trends are reported for the central cell. According to available data, several minutes are needed to reach operational conditions. Therefore, a quasi-steady state assumption was considered acceptable for the start-up analysis.

The presented results can be discussed considering that if also a little amount of the top flow is able to reach the cell, this may cause an increase of the temperature where stagnation occurs. At start-up, if this undesired recirculation does not occur, the maximum values of temperature are about 337 K (64 °C), for both anode and cathode. What is highlighted once more by this different operational case is that hot spots occur at the side of the cell where fluid velocity is lower. For such case, temperature values are more comparable to the ones of 115th cell, in contrast to the significant differences among cells highlighted in Fig. 10.

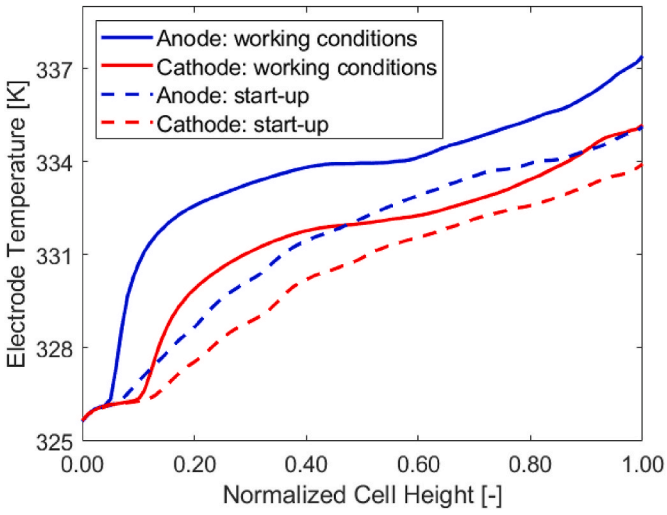

Fig. 14. Anode and cathode temperature for the central cell at start-up and during operation.

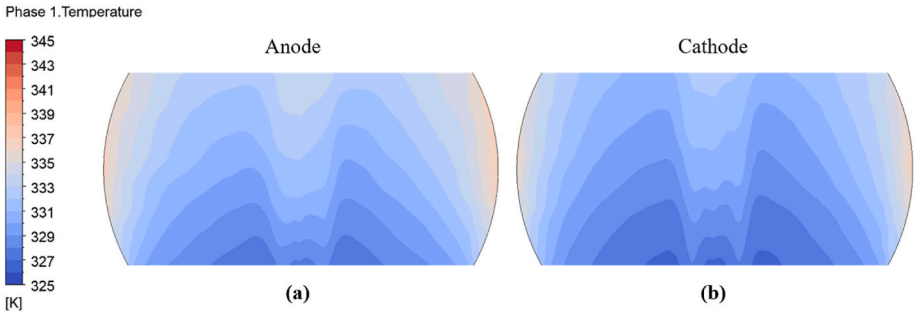

Fig. 13. Central cell contours with start-up temperature: thermal behaviour of anode (**a**) and cathode (**b**).

The chart of Fig. 14 presents the temperature trend on both electrodes for the start-up case, comparing it to the operating case. The temperatures are on average 3 K lower for the anode and 1.5 K for the cathode, during the start-up phase. Also, temperature rises more smoothly and linearly with the cell height during start-up, compared to the working conditions trend.

5. Discussion

A high-fidelity, multi-physics CFD model for alkaline water electrolyzers was presented, addressing key limitations in the existing literature and providing valuable insights on the main variables of interest. The developed model integrates two-phase flow, electrochemical reactions, and thermal dynamics, including Joule and Faraday heating, enabling realistic simulations. By incorporating a full-cell geometry with a diaphragm, it overcomes simplifications commonly found in prior studies, which often neglect geometric and multi-physics complexities.

The model's calibration of boundary conditions allowed realistic simulation of individual cells within a stack, accounting for variations in pressure and mass flows, tailoring the conditions to the specific cell at hand. Furthermore, the inclusion of the diaphragm significantly enhanced the accuracy of thermal predictions by promoting uniform temperature distribution. The results discussion is divided below in subsection, to highlight the main topics investigated.

5.1. Diaphragm influence on the cell simulation

When conducting CFD simulations on electrolyzer cells, the exclusion of the diaphragm, as in standalone half-cell models, leads to increased localized heating and gas accumulation. For the case-study analyzed, comparisons between cases with and without the diaphragm revealed that excluding the diaphragm led to higher localized heating, with a difference in maximum temperature of 10 K. More gas accumulation, monitored through the gas volume fraction, was also noticed in the non-diaphragm case, confirming the diaphragm's pivotal role in realistic simulations. Higher recirculation, observed when including the diaphragm, promoted uniform temperature distribution within the cell by enhancing mixing and reducing thermal gradients.

5.2. Gas distribution at electrodes along the stack

When studying a single cell, a volume fraction disparity between cathode and anode is expected. More specifically, cathode VF can be from 25 % to 30 % higher than anode VF. This behaviour, that can be attributed to the different densities of hydrogen and oxygen, has to be considered for the design phase. When dealing with risk management, cathodic half cell may be a more critical component than the anodic one, for this reason. The VF disparity between half-cell leads to distinct flow patterns. At the stack level, last cells can be disadvantaged, with higher gas accumulation, due to the lower mass flow reaching them, leading to higher stagnation.

For the specific case-study electrolyzer at hand, a gas VF value of 0.48 was reported for all the cells' cathodes. At the anode, a gas volume fraction discrepancy among cells was observed: the first and central cells shared a value of 0.34, while the last cell had a value of 0.39, mainly attributed to different flow channeling entering the last cell. Vertical velocity analysis indicated variable fluid-dynamic patterns in the bottom regions of the cells.

5.3. Thermal analysis

Higher temperatures are found to occur at the anode than at the cathode and hot spots are particularly evident in regions of electrolyte stagnation. Two reasons were hypothesized: first, the two gases have a different specific heat at working temperatures and pressures, with the hydrogen gas at the cathode less prone to increase its temperature; second, velocity non-uniformity in the two half-cells showed that slower flows are generally associated with higher temperatures. Hot spots for the specific case were evident in regions of gas accumulation, where the electrolyte stagnates, with maximum values at the first cell anode being 15 K higher than the expected outlet temperature of 343.15 K. Thermal disparities among cells were mainly influenced by top channel effects. Simulations in start-up conditions (top channel temperatures at 325.15 K) reduced anode temperatures by 3 K and cathode temperatures by 1.5 K on average.

6. Conclusions

This study presents a 3D multi-physics CFD model for alkaline water electrolyzer cells, integrating bubble coverage and heating sources from electrochemical processes, addressing key gaps in the literature. Furthermore, different cells within the stack were simulated by applying tailored boundary conditions. The close agreement between simulated and expected temperatures confirmed the model's reliability and its applicability for design optimization.

The main take-home messages of the study are reported below.

- The exclusion of the diaphragm, as in standalone half-cell models, leads to increased localized heating and gas accumulation. Therefore, incorporating the diaphragm is essential for accurate and realistic simulations.
- At the cell level, a difference in volume fraction between the cathode and anode is reported, with the cathode's volume fraction potentially being 25%–30% higher than that of the anode. At the stack level, the last cells may experience a disadvantage, resulting in greater gas accumulation, due to the reduced mass flow reaching them, which leads to higher stagnation. Thus, when dealing with gas accumulation, cathodic cells are the ones to be more carefully designed and monitored.
- Lower velocities at the electrodes result in higher local temperatures. By performing the CFD simulations on the cell, hot spots were identified, primarily caused by velocity non-uniformity and stagnant electrolyte, highlighting the necessity of a multi-physics approach that includes thermal analysis. When dealing with the thermal analysis, anodic cells are the ones to be more carefully designed and monitored, to avoid high temperatures.

While this research focuses on conventional cell designs, it establishes a foundation for studying advanced configurations, such as zero-gap cells. Future work could explore other topics of interest, such as long-term degradation effects, innovative designs to mitigate hot spots, adaptation of this modeling approach for next-generation electrolyzer technologies.

By improving efficiency, safety, and scalability, this study contributes to advancing green hydrogen production.

CRediT authorship contribution statement

Marco Dreoni: Writing – original draft, Methodology, Investigation, Formal analysis, Data curation, Conceptualization. **Francesco Balduzzi:** Writing – review & editing, Validation, Supervision, Project administration, Methodology, Conceptualization. **Francesco Maria Ferro:** Writing – review & editing, Supervision, Conceptualization. **Kevin Panichi:** Writing – review & editing, Supervision. **Eleonora Ponticorvo:** Supervision. **Giovanni Ferrara:** Visualization, Funding acquisition. **Alessandro Bianchini:** Writing – review & editing, Supervision, Project administration, Funding acquisition, Conceptualization.

Declaration of competing interest

The authors declare that they have no known competing financial

interests or personal relationships that could have appeared to influence the work reported in this paper.

References

[1] Rodríguez J, Amores E. CFD modeling and experimental validation of an alkaline water electrolysis cell for hydrogen production. Processes Dec. 2020;8(12). https://doi.org/10.3390/pr8121634. Art. no. 12.

[2] Wang T, Wang J, Wang P, Wang F, Liu L, Guo H. Non-uniform liquid flow distribution in an alkaline water electrolyzer with concave-convex bipolar plate (CCBP): a numerical study. Int. J. Hydrog. Energy Apr. 2023;48(33):12200–14. https://doi.org/10.1016/j.ijhydene.2022.12.203.

[3] Ulleberg Ø. Modeling of advanced alkaline electrolyzers: a system simulation approach. Int. J. Hydrog. Energy Jan. 2003. https://doi.org/10.1016/S0360-3199(02)00033-2.

[4] Gao LY, Yang L, Wang CH, Shan GX, Huo XY, Zhang MF, Li W, Zhang JL. Three-dimensional two-phase CFD simulation of alkaline electrolyzers. J. Electrochem 2023;29(3). https://doi.org/10.13208/j.electrochem.2207081.

[5] Muhsen H, Alshawabkeh M, Al-Mahmodi M, Ghanem A, Al-Halhouli A. Sensitivity analysis of electrodes spacing media for evaluating alkaline electrolyzer performance through CFD modeling. Renew. Energy Focus Jun. 2024;49:100575. https://doi.org/10.1016/j.ref.2024.100575.

[6] Norazahar N, Khan F, Rahmani N, Ahmad A. Degradation modelling and reliability analysis of PEM electrolyzer. Int. J. Hydrog. Energy Jan. 2024;50:842–56. https://doi.org/10.1016/j.ijhydene.2023.07.153.

[7] Mat MD, Aldas K, Ilegbusi OJ. A two-phase flow model for hydrogen evolution in an electrochemical cell. Int. J. Hydrog. Energy Aug. 2004;29(10):1015–23. https://doi.org/10.1016/j.ijhydene.2003.11.007.

[8] Xue L, Song S, Chen W, Liu B, Wang X. Enhancing efficiency in alkaline electrolysis cells: optimizing flow channels through multiphase computational fluid dynamics modeling. Energies Jan. 2024;17(2). https://doi.org/10.3390/en17020448. Art. no. 2.

[9] Lee J, Alam A, Ju H. Multidimensional and transient modeling of an alkaline water electrolysis cell. Int. J. Hydrog. Energy Apr. 2021;46(26):13678–90. https://doi.org/10.1016/j.ijhydene.2020.10.133.

[10] Muthiah M, Elnashar M, Afzal W, Tan H. Safety assessment of hydrogen production using alkaline water electrolysis. Int. J. Hydrog. Energy 2024;84:803–21. https://doi.org/10.1016/j.ijhydene.2024.08.237.

[11] Haoran C, Xia Y, Wei W, Yongzhi Z, Bo Z, Leiqi Z. Safety and efficiency problems of hydrogen production from alkaline water electrolyzers driven by renewable energy sources. Int. J. Hydrog. Energy 2024;54:700–12. https://doi.org/10.1016/j.ijhydene.2023.08.324.

[12] Liu Y, Amin MT, Khan F, Pistikopoulos EN. Safety analysis of proton exchange membrane water electrolysis system'. J Environ Chem Eng 2023;11(5). https://doi.org/10.1016/j.jece.2023.110772.

[13] Alam A, Park C, Lee J, Ju H. Comparative analysis of performance of alkaline water electrolyzer by using porous separator and ion-solvating polybenzimidazole membrane. Renew Energy Apr. 2020;166:222–33. https://doi.org/10.1016/j.renene.2020.11.151.

[14] Hawkes G, O'Brien J, Stoots C, Hawkes B. 3D CFD model of a multi-cell high-temperature electrolysis stack. Int. J. Hydrog. Energy May 2009;34(9):4189–97. https://doi.org/10.1016/j.ijhydene.2008.11.068.

[15] Olesen AC, Frensch SH, Kær SK. Towards uniformly distributed heat, mass and charge: a flow field design study for high pressure and high current density operation of PEM electrolysis cells. Electrochim Acta Jan. 2019;293:476–95. https://doi.org/10.1016/j.electacta.2018.10.008.

[16] Dreoni M, Balduzzi F, Ferro FM, Neben M, Hossain SS, Ferrara G, Bianchini A. Alkaline electrolysis CFD modeling and application: a novel expression for a volume fraction-dependent current density. Proceedings of the 37th international conference on efficiency, cost, optimization, simulation and environmental impact of energy systems (ECOS). 30 June–4 July 2024. Rhodes, Greece.

[17] Dreoni M, Balduzzi F, Ferrara G, Bianchini A. Accuracy assessment of the eulerian two-phase model for the CFD simulation of gas bubbles dynamics in alkaline electrolyzers. J. Phys.: Conf. Ser 2022;2385:012040.

[18] Dreoni M, Balduzzi F, Hossain SS, Neben M, Ferro FM, Ferrara G, Bianchini A. Definition of critical metrics for performance evaluation and multiphase flow modeling in an alkaline electrolyzer using CFD. Energies Jan. 2024;17(21). https://doi.org/10.3390/en17215317. Art. no. 21.

[19] ANSYS fluent theory guide. Available online: https://dl.cfdexperts.net/cfd_resources/Ansys_Documentation/Fluent/Ansys_Fluent_Theory_Guide.pdf. [Accessed 1 December 2024].

[20] Frey F. Experimental set-up for bubble behaviour in a high pressure alkaline electrolyte. Karlsruhe, Germany: Karlsruhe Institute of Technology; 2016. Master Thesis.

[21] Hreiz R, Abdelouahed L, Fünfschilling D, Lapicque F. Electrogenerated bubbles induced convection in narrow vertical cells: PIV measurements and euler–Lagrange CFD simulation. Chem Eng Sci 2015;134:138–52. https://doi.org/10.1016/j.ces.2015.04.041.

[22] Haug P, Kreitz B, Koj M, Turek T. Process modelling of an alkaline water electrolyzer. Int. J. Hydrog. Energy Jun. 2017;42(24):15689–707. https://doi.org/10.1016/j.ijhydene.2017.05.031.

[23] Mei X, Yuan S, Zhao C, Yan X, Zhao C, Wang Q. Measuring three-dimensional bubble dynamics for hydrogen production via water electrolysis. Phys Fluids Dec. 2023;35(12):123338. https://doi.org/10.1063/5.0173622.

[24] Hoedemakers I. Study of the bubble behavior in alkaline water electrolysis. Eindhoven, The Netherlands: Eindhoven University of Technology; 2020. Master Thesis.

[25] Antal SP, Lahey RT, Flaherty JE. Analysis of phase distribution in fully developed laminar bubbly two-phase flow. Int. J. Multiph. Flow Sep. 1991;17(5):635–52. https://doi.org/10.1016/0301-9322(91)90029-3.

[26] Diéguez PM, Ursúa A, Sanchis P, Sopena C, Guelbenzu E, Gandía LM. Thermal performance of a commercial alkaline water electrolyzer: experimental study and mathematical modeling. Int. J. Hydrog. Energy Dec. 2008;33(24):7338–54. https://doi.org/10.1016/j.ijhydene.2008.09.051.

[27] Onda K, Kyakuno T, Hattori K, Ito K. Prediction of production power for high-pressure hydrogen by high-pressure water electrolysis. J Power Sources May 2004;132(1):64–70. https://doi.org/10.1016/j.jpowsour.2004.01.046.

[28] Marini S, et al. Advanced alkaline water electrolysis. Electrochim Acta Nov. 2012;82:384–91. https://doi.org/10.1016/j.electacta.2012.05.011.

[29] Benghanem M, Almohamadi H, Haddad S, Mellit A, Chettibi N. The effect of voltage and electrode types on hydrogen production powered by photovoltaic system using alkaline and PEM electrolyzers. Int. J. Hydrog. Energy Feb. 2024;57:625–36. https://doi.org/10.1016/j.ijhydene.2023.12.232.

[30] Sakas G, Ibáñez-Rioja A, Ruuskanen V, Kosonen A, Ahola J, Bergmann O. Dynamic energy and mass balance model for an industrial alkaline water electrolyzer plant process. Int. J. Hydrog. Energy Jan. 2022;47(7):4328–45. https://doi.org/10.1016/j.ijhydene.2021.11.126.

[31] Henkensmeier D, et al. Separators and membranes for advanced alkaline water electrolysis. Chem. Rev. May 2024;124(10):6393–443. https://doi.org/10.1021/acs.chemrev.3c00694.

[32] Brauns J, et al. Evaluation of diaphragms and membranes as separators for alkaline water electrolysis. J Electrochem Soc Jan. 2021;168(1):014510. https://doi.org/10.1149/1945-7111/abda57.